

A Front-End ASIC With High-Voltage Transmit Switching and Receive Digitization for 3-D Forward-Looking Intravascular Ultrasound Imaging

Tan, Mingliang; Chen, Chao; Chen, Zhao; Janjic, Jovana; Daeichin, Varya; Chang, Zu-Yao; Noothout, Emile; van Soest, Gijs; Verweij, Martin D.; de Jong, Nico

DOI

[10.1109/JSSC.2018.2828826](https://doi.org/10.1109/JSSC.2018.2828826)

Publication date

2018

Document Version

Accepted author manuscript

Published in

IEEE Journal of Solid State Circuits

Citation (APA)

Tan, M., Chen, C., Chen, Z., Janjic, J., Daeichin, V., Chang, Z.-Y., Noothout, E., van Soest, G., Verweij, M. D., de Jong, N., & Pertijs, M. A. P. (2018). A Front-End ASIC With High-Voltage Transmit Switching and Receive Digitization for 3-D Forward-Looking Intravascular Ultrasound Imaging. *IEEE Journal of Solid State Circuits*, 53(8), 2284-2297. <https://doi.org/10.1109/JSSC.2018.2828826>

Important note

To cite this publication, please use the final published version (if applicable).
Please check the document version above.

Copyright

Other than for strictly personal use, it is not permitted to download, forward or distribute the text or part of it, without the consent of the author(s) and/or copyright holder(s), unless the work is under an open content license such as Creative Commons.

Takedown policy

Please contact us and provide details if you believe this document breaches copyrights.
We will remove access to the work immediately and investigate your claim.

A Front-End ASIC with High-Voltage Transmit Switching and Receive Digitization for 3D Forward-Looking Intravascular Ultrasound Imaging

Mingliang Tan, Chao Chen, *Member, IEEE*, Zhao Chen, Jovana Janjic, Verya Daeichin, Zu-yao Chang, *Member, IEEE*, Emile Noothout, Gijs van Soest, *Member, IEEE*, Martin D. Verweij, *Member, IEEE*, Nico de Jong, *Member, IEEE*, and Michiel A. P. Pertijs, *Senior Member, IEEE*

Abstract— This paper presents an area- and power-efficient ASIC for 3D forward-looking intravascular ultrasound imaging. The ASIC is intended to be mounted at the tip of a catheter, and has a circular active area with a diameter of 1.5 mm on top of which a 2D array of piezo-electric transducer elements is integrated. It requires only 4 micro-coaxial cables to interface 64 receive (RX) and 16 transmit (TX) elements with an imaging system. To do so, it routes high-voltage (HV) pulses generated by the system to selected TX elements using compact HV switch circuits, digitizes the resulting echo signal received by a selected RX element locally, and employs an energy-efficient load-modulation datalink to return the digitized echo signal to the system in a robust manner. A multi-functional command line provides the required sampling clock, configuration data and supply voltage for the HV switches. The ASIC has been realized in a 0.18 μm HV CMOS technology and consumes only 9.1 mW. Electrical measurements show 28 V HV switching and RX digitization with a 16 MHz bandwidth and 53 dB dynamic range. Acoustical measurements demonstrate successful pulse transmission and reception. Finally, a 3D ultrasound image of a 3-needle phantom is generated to demonstrate the imaging capability.

Index Terms—intravascular ultrasound imaging, piezo-electrical transducer, high-voltage switching, receive digitization, cable-count reduction.

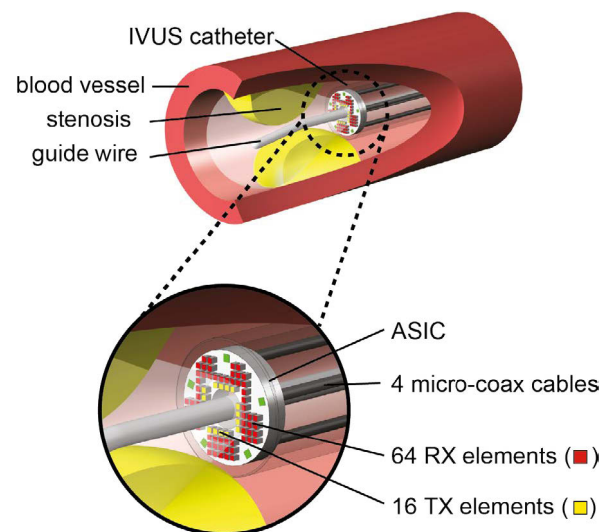


Fig. 1. A conceptual diagram of the forward-looking IVUS catheter.

I. INTRODUCTION

CORONARY artery disease is caused by atherosclerosis of the coronary arteries of the heart [1]. It has become one of the most common causes of death worldwide [2]. Intravascular ultrasound (IVUS) imaging, using an ultrasound transducer mounted at the tip of a catheter, is an important tool for the visualization, diagnosis and treatment of atherosclerosis [3].

Conventional IVUS catheters are side-looking (SL) devices that provide a 2D cross-sectional image of the vessel wall. An ultrasound transducer mounted at the tip of the catheter is excited by high-voltage pulses to generate an acoustic pulse, and the resulting echo signals are processed to form the image. IVUS catheters employ either a mechanically-rotating single-element transducer [4], or 64 elements folded around the tip of the catheter [5, 6]. Mechanical rotation is complex to implement, and relatively slow, leading to motion artefacts in the image [7], while the use of a transducer array comes with an electrical interconnect challenge due to the limited number of cables that can be accommodated in a catheter shaft.

M. Tan Z. Chen, Z. Chang and M. A. P. Pertijs are with the Electronic Instrumentation Lab, Delft University of Technology, Delft, The Netherlands (e-mail: m.tan@tudelft.nl).

C.Chen was with the Electronic Instrumentation Lab, Delft University of Technology, Delft 2628 CD, The Netherlands. He is currently with Butterfly Network Inc., Guilford, CT 06437, USA.

J. Janjic and G. van Soest are with the Thoraxcenter, Department of Biomedical Engineering, Erasmus University Medical Center, Rotterdam 3015 CN, The Netherlands.

E. Noothout is with the Laboratory of Acoustical Wavefield Imaging, Delft University of Technology, Delft 2628 CJ, The Netherlands.

M. D. Verweij and N. de Jong are with the Laboratory of Acoustical Wavefield Imaging, Department of Imaging Physics, Delft University of Technology, Delft 2628 CJ, The Netherlands, and also with the Thoraxcenter, Department of Biomedical Engineering, Erasmus University Medical Center, Rotterdam 3015 CN, The Netherlands.

A severe case of coronary artery disease is a chronic total occlusion, a condition in which atherosclerotic plaque completely blocks the vessel. Successful recanalization of such occlusions using guidewires is associated with improved left ventricular function and reduced mortality [8, 9]. For this type of lesions, forward-looking (FL) imaging is required, since imaging ahead of the catheter tip can help to distinguish between plaque and normal vessel wall during the crossing procedures, hence reducing the risks of dissections and vessel perforation [3].

Early implementations of FL-IVUS catheters are based on the scanning motion of a FL single-element transducer [10, 11] or a rotating single element oriented at 45° angle [12]. Both implementations require rotation and multiple acquisitions to construct a 2D image, and are sensitive to motion artifacts. In order to achieve real-time forward-looking 3D imaging without rotation, a circular transducer array [13, 14], or a 2D transducer array [15] can be placed at the tip of the catheter. However, connecting the resulting relatively large number of elements (50-100) using micro-coaxial cables within the catheter diameter of < 2 mm is extremely challenging.

ASICs for FL-IVUS have been reported that employ pulsed and multiplexers to reduce the number of cables, but these still require at least 13 connections [13, 14, 16]. Moreover, they communicate the received echo signals to the imaging system in an analog form, which is relatively susceptible to interference and not amenable to digital multiplexing or data-reduction approaches. Also, the use of wireless data transmission has been proposed to reduce the cable count [17], but the integration of the required antenna on a catheter is challenging, and successful wireless operation on a catheter is yet to be demonstrated.

This paper presents a front-end ASIC that requires only 4 micro-coaxial cables to interface with a total of 80 piezoelectric transducer elements fabricated on top of the ASIC: 64 receive (RX) elements and 16 transmit (TX) elements [18]. In contrast with prior work, the ASIC digitizes the received echo signals locally, allowing their transmission to an external imaging system in a robust form, and demonstrating the feasibility of in-probe digitization within the stringent size, power and interconnect constraints of a FL-IVUS probe. The ASIC has been designed for FL-IVUS, but the presented approaches to in-probe digitization, cable-count reduction and high-voltage switching are equally applicable in a SL-IVUS probe, or in other miniature probes, such as intracardiac echography (ICE) catheters.

Fig. 1 illustrates conceptually how the ASIC will be mounted at the tip of a catheter. The ASIC will be laser-cut into a donut shape, with an outer diameter of 1.5 mm and an inner hole of 0.5 mm for the guide wire. The ASIC enables synthetic aperture imaging, in which acoustic pulses are transmitted using one or multiple TX elements, and the resulting received echoes are recorded by one RX element at a time. Expanding on our earlier publication [18], which reports preliminary results obtained using a test transducer array that is connected to the ASIC using wire bonds, this paper presents

TABLE I. Key parameters of the applied transducer elements.

Size	80 $\mu\text{m} \times 80 \mu\text{m}$
Resonance Frequency	13 MHz
-3 dB Bandwidth	44% (10 MHz ~ 16 MHz)
Impedance at Resonance	0.7 pF // 5 k Ω
Transmit Efficiency	0.4 kPa/V @ 6 mm
Receive Sensitivity	4 $\mu\text{V}/\text{Pa}$

a detailed description of the design and new experimental results obtained with transducer elements integrated on top of the ASIC.

This paper is organized as follows. Section II describes the proposed system architecture. Section III discusses the details of the circuit implementation. Sections IV and V present the experimental results and conclusions.

II. SYSTEM ARCHITECTURE

A. Transducer Array

FL-IVUS probes have been reported that apply a ring-shaped transducer array based on Capacitive Micromachined Ultrasonic Transducers (CMUTs) [13, 14] or a 2D matrix

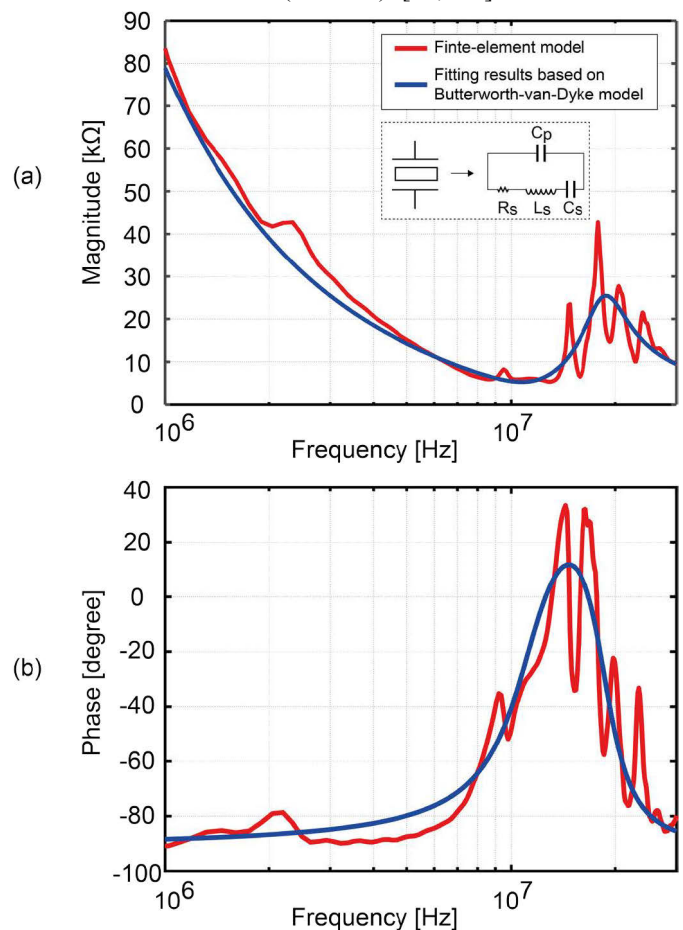


Fig. 2. Simulated impedance characteristics obtained using finite-element modeling, and the fitting results based on the Butterworth-van-Dyke model: (a) magnitude versus frequency; (b) phase versus frequency.

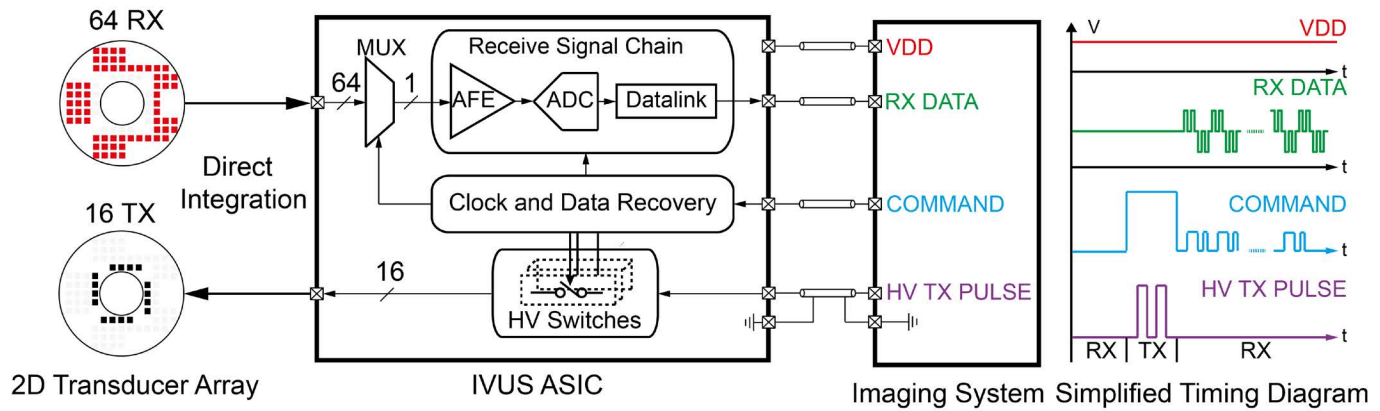


Fig. 3. Block diagram of the IVUS ASIC.

array based on piezo-electrical (PZT) transducers [15]. These designs either have a relatively low signal to noise ratio or require a large number of cables to be integrated. To overcome these limitations, we have developed a PZT-based matrix transducer with a total of 80 elements only needing 4 coaxial cables to be integrated inside a catheter. The transducer elements for transmit and receive are separated (16 for TX and 64 for RX), as illustrated in Fig. 1. The transducer array built on top of the ASIC uses the approach described in [19].

We employ $80 \mu\text{m} \times 80 \mu\text{m}$ transducer elements with a pitch of $100 \mu\text{m}$. The center frequency of these elements is 13 MHz. This is lower than the frequencies typically used in SL-IVUS devices, which operate at 20 MHz or above [5, 6]. The chosen frequency is comparable to earlier FL-IVUS designs, e.g. [14, 20], and trades off resolution for larger penetration depth as required in forward-looking imaging. The -3 dB bandwidth of the elements is 44% (10 MHz ~ 16MHz). The impedance characteristic of the transducer elements has been simulated using finite-element analysis software (PZFlex LLC, Cupertino), as shown in Fig. 2. This simulation includes the whole transducer stack (PZT, matching layer, ASIC, glue, ground foil). Since the element thickness of $80 \mu\text{m}$ is close to the wavelength ($100 \mu\text{m}$), various mode vibrations occur in the different layers, resulting in fluctuations of the impedance as function of the frequency. To obtain a lumped-element model suitable for circuit simulation, we approximate the electrical impedance around resonance by a Butterworth-Van Dyke lumped-element model (also shown in Fig. 2), which captures the main resonance mode and the element's electrical capacitance. The parameters of this model are obtained by means of least-squares curve fitting on the simulated impedance data. The transducer's impedance at resonance is approximately $0.7 \text{ pF} // 5 \text{ k}\Omega$. The elements have a measured transmit efficiency of 0.4 kPa/V at 6 mm from the transducer. Their measured receive sensitivity is around $4 \mu\text{V/Pa}$. To generate sufficient acoustic pressure to be able to detect the low backscattered signal from blood [21] at an imaging depth suitable for FL-IVUS, transmit voltages on the order of 30 V are required. Table I summarizes the key parameters of the applied transducer.

While a matrix of transducer elements covering the full ASIC would be best for imaging, we leave out elements to

make space for five bond pads, which provide electrical connections (one of which is a ground) to four micro-coaxial cables. In the prototype presented in this paper, the ASIC is connected using wire bonds on the same side as the transducer elements, but these can be replaced in the future by through-silicon vias to realize more convenient connections on the back side of the ASIC. Elements are also omitted in the center of the ASIC to make room for the catheter's guide wire.

The 80 elements are divided into 16 transmit (TX) elements and 64 receive (RX) elements. The transmit elements are located around the guide wire hole, while the receive elements cover a larger aperture and determine the lateral imaging resolution. This partitioning allows the receive circuitry to be implemented using compact low-voltage circuitry, while the number of high-voltage circuits associated with the transmit elements, which occupy a relatively large die size, is kept limited.

B. ASIC Architecture

Fig. 3 shows the top-level architecture of the proposed ASIC. The ASIC consists of three main parts: 1) high-voltage (HV) switches, 2) a receive signal chain, and 3) a clock and data recovery circuit.

The HV switches are responsible for exciting the 16 TX elements using HV pulses in order to generate enough acoustic pressure. Several implementations of on-chip HV pulsers have been reported that can serve this purpose [22, 23]. Pulsers employing a resistive pull-up to a HV supply [13] are simple and area-efficient, but are relatively power hungry due to the current flowing through the pull-up resistor. A push-pull architecture [22] is more power-efficient, but requires more HV transistors to implement a level shifter to control the pull-up transistor and thus occupies more die area. An alternative to using on-chip pulsers is to use on-chip switches to route an externally-generated HV signal (HV TX PULSE in Fig. 3) to selected transducer elements [24]. This approach reduces the on-chip power dissipation and allows the use of arbitrary transmit waveforms. We present an area-efficient HV switch implementation, by means of which one or more of the TX elements can be connected via a TX cable to the imaging system. This allows for the implementation of a synthetic-aperture transmit scheme, in which each of the 16 TX elements are successively pulsed, or, alternatively, a plane-

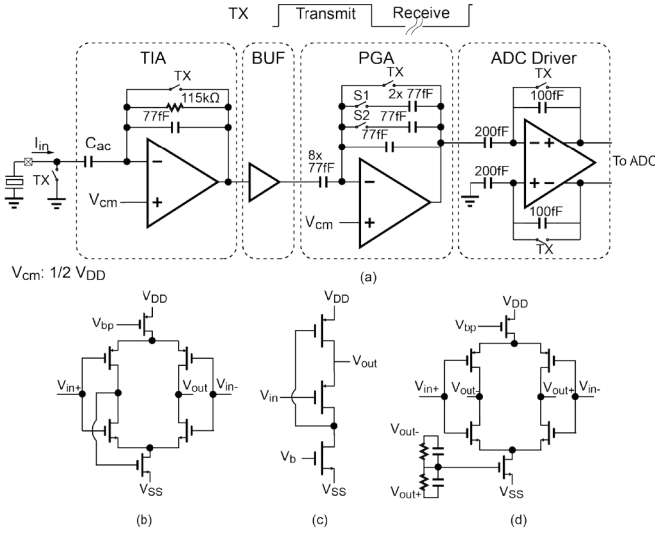


Fig. 4. Circuit diagrams of (a) the analog front-end; (b) the OTA used in both the TIA and the PGA; (c) the buffer stage; and (d) the OTA of the ADC driver.

wave transmit scheme, in which multiple TX elements are pulsed simultaneously.

The receive signal chain is responsible for transferring the received echo signals to the imaging system. In contrast with prior analog approaches [13, 14], we digitize the echo signals locally. In order to do so, we connect one of the 64 RX elements via an analog multiplexer and an analog front-end circuit to an ADC. This allows for the implementation of a synthetic-aperture receive scheme, in which the echo signals received by the 64 RX elements are digitized in 64 successive pulse-echo sequences. Combined with the synthetic-aperture transmit scheme, a complete synthetic-aperture image can be obtained in 1024 (16×64) sequences. The estimated volume frame rate is on the order of 100 fps for an imaging depth of 8 mm. While this is sufficient for our application, higher frame rates could be achieved by using multiple analog front-ends and ADCs and less multiplexing. This, however, comes with the challenges of increased die size and output data rates.

The analog front-end circuit amplifies the echo signal with a programmable gain to match it to the input range of the ADC. To detect the low backscattered signal from blood, an ultrasound system requires a dynamic range (DR) of at least 70 dB [21]. The DR of the receive signal chain can be lower than this, because the beamforming operation that combines the 16×64 receive signals to form the image enhances the DR. In the case of full synthetic phased array imaging, the DR will increase by $\sqrt{(16 \cdot 64)}$, or 30 dB, while other imaging schemes can provide even more [25]. To reach an overall DR of 80 dB, we aim for a DR of 50 dB per channel. Considering this DR requirement and the 13 MHz transducer center frequency, a 60-MS/s 10-bit SAR ADC is adopted. The ADC's output data is transmitted serially to the imaging system using a load-modulation-based data link (RX DATA).

The clock and data recovery circuit is responsible for extracting the ADC sampling clock and the pulse-width encoded configuration data, including the switch and gain settings, from a COMMAND signal generated by the imaging

system during the RX phase. This same signal is also used to distinguish between the TX and the RX phases. During TX, the line is pulled to 5 V by the system, providing a supply voltage for the HV transmit circuit, as will be discussed in Section III-D.

In addition to the three mentioned cables (HV TX PULSE, RX DATA and COMMAND), a fourth cable provides the ASIC with a supply voltage (VDD) of 1.9 V.

III. CIRCUIT IMPLEMENTATION

A. Analog Front-End

Fig. 4a shows the circuit diagram of the analog front-end (AFE), which converts the signal current of the selected RX element to a differential input voltage for the ADC. It consists of a trans-impedance amplifier (TIA), a buffer stage (BUF), a programmable-gain amplifier (PGA) and an ADC driver. Note that the multiplexer at the input has been omitted in this figure for simplicity.

The TIA is used to amplify the signal current I_{in} produced by the small PZT elements. Considering, as shown in Fig. 2, the relatively high source resistance ($\sim 5 \text{ k}\Omega$) and the small capacitance ($\sim 0.7 \text{ pF}$), a trans-impedance amplifier (TIA) is a power-efficient circuit topology. We opt for a single-ended TIA in view of the inherently single-ended nature of the transducer elements, due to the common ground electrode shared by all elements. A fully-differential implementation would require more area, while the benefit of lower harmonic distortion is not critical in our application, since harmonics are out-of-band and will be filtered out. The TIA senses the signal current I_{in} and converts it into an output voltage. A feedback resistor of 115 k Ω sets the trans-impedance gain, while a feedback capacitor of 77 fF ensures stability and sets the -3 dB bandwidth to 18 MHz.

To make the DC biasing of the TIA's virtual ground independent of that of the transducer, a coupling capacitor C_{ac} of 5.6 pF is used. This allows the transducer to be shorted to ground during the TX phase and connected to the TIA during the RX phase, without voltage transients that lead to parasitic acoustic transmissions. During the TX phase, the TIA's feedback network is shorted, thus keeping the amplifier in unity-gain feedback and preventing parasitic on-chip coupling of the HV transmit pulse from affecting the receive path.

A current-reuse operational transconductance amplifier (OTA) is employed to increase the power-efficiency of the TIA, as shown in Fig. 4b [26]. The applied differential architecture allows the use of a tail-current source that isolates the signal-path from interfering signals superimposed on the supply voltage. The OTA is biased at 220 μA to ensure that the TIA's bandwidth covers the transducer's bandwidth and that the input-referred noise of the receive signal chain is dominated by the transducer (whose in-band rms noise is around 4.4 nA) rather than the TIA. The OTA's non-inverting input is biased at a mid-supply reference voltage V_{cm} , using a resistive divider (not shown).

The PGA is implemented as an inverting amplifier with a switchable capacitive feedback network, which provides a

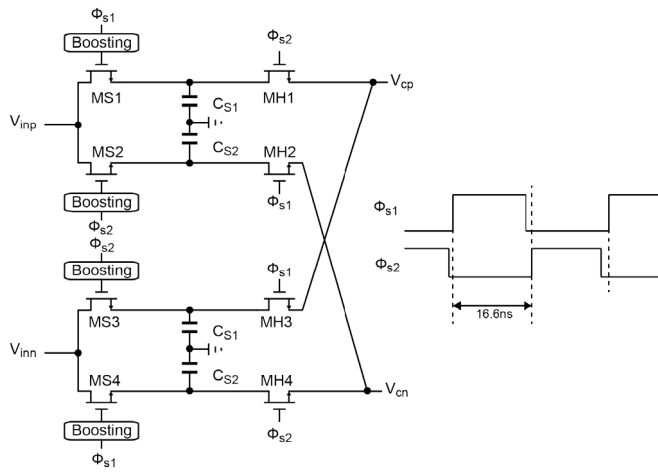


Fig. 7. Circuit diagram of two-path time interleaved sampling.

capacitors, one is pre-charged to the reference voltage, after which successive charge redistribution with the other 3 is used to create the 3 least-significant reference charges (0.5:0.25:0.125) [31]. A unit capacitor C_u of 32 fF is used to meet the 10-bit matching requirement, taking into account both matching between the unit capacitors and the effect of parasitic capacitance of the switches controlled by CP and CN shown in Fig. 5. This leads to total CDAC capacitance of 2 pF. As said, the sampling capacitors C_s are of the same size. The associated kT/C noise is well below the LSB step of the ADC.

A self-timed architecture is implemented for the SAR logic to avoid the need of an oversampled clock. Via the COMMAND line, an external 60 MHz clock is used to trigger the start of the conversion. The comparator clock is generated by asynchronous SAR logic. In order to increase the linearity of the input sampling switches, the drive signal of these NMOS switches is boosted to achieve an over-drive voltage of ~ 1.3 V [32]. The power consumption of the ADC is fully dynamic and amounts to 2.8 mW.

Fig. 6 shows the schematic of the reference buffer. A reference voltage $V_{ref,in}$ of 0.3 V is derived from the supply voltage V_{DD} by means of a resistive divider comprised of R_1 and R_2 . While this means that any variation in V_{DD} results in a variation of $V_{ref,in}$ with an attenuation of only $6\times$ (16 dB), this is not problematic, since the chip's supply voltage is directly provided from the system side via one of the four cables (see Fig. 3). There, a voltage regulator is used to stabilize the DC value of the supply voltage. To prevent high-frequency signals on the supply from coupling into the reference voltage, an on-chip bypass capacitor C_f is included. An OTA and a source follower form an op-amp which is configured as a unity-gain stage and forces V_{ref} equal to $V_{ref,in}$. A scaled replica stage comprised of M_2 and R/m , charges the CDAC in an open-loop manner to a reference voltage V_{ref} that tracks V_{ref} and hence $V_{ref,in}$. The scale factor $m = 10$ is chosen to ensure sufficient CDAC settling. Only 39 μA is consumed in the OTA and 60 μA in the source follower comprised of M_1 and R . 600 μA is consumed in the replica stage to ensure low enough output impedance for sufficient CDAC settling.

In order to reduce the power consumption of the ADC

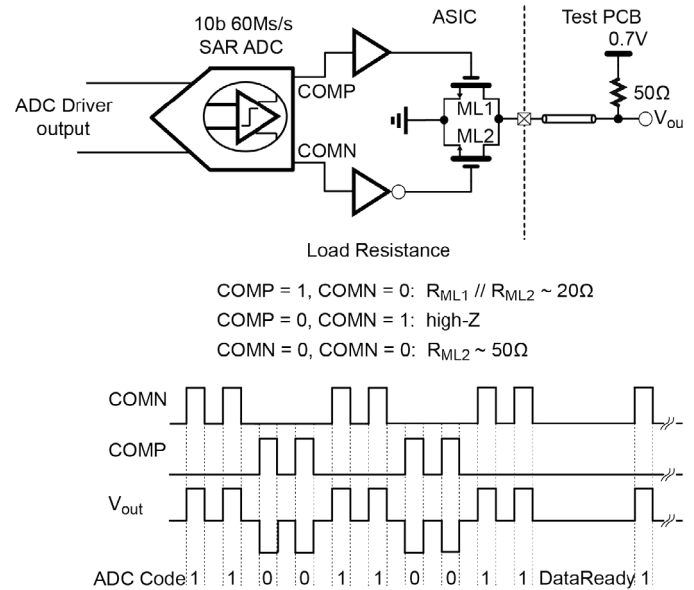


Fig. 8. Circuit diagram and waveforms for the load modulation datalink.

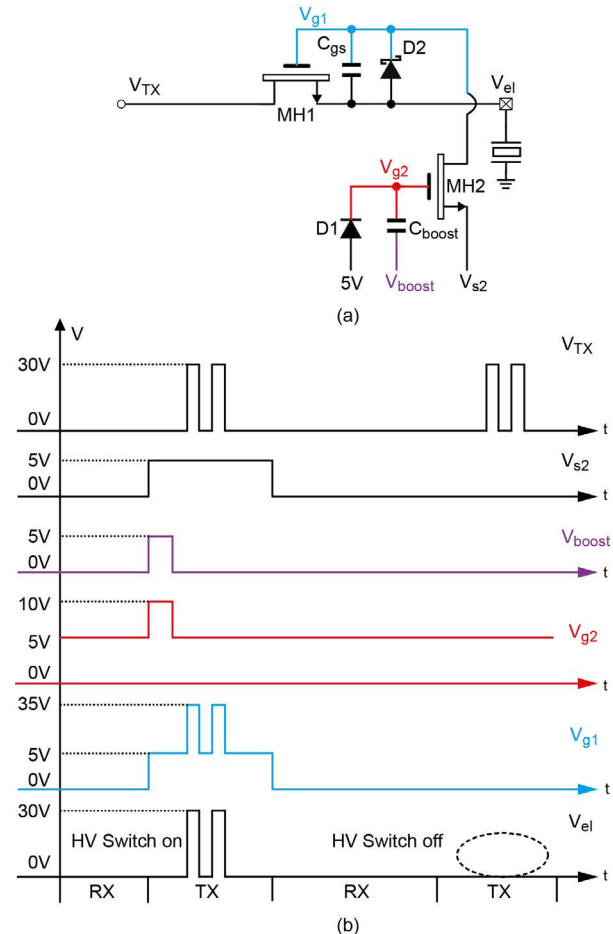


Fig. 9. (a) Conceptual diagram of the high-voltage switch circuit; (b) The associated timing diagram.

driver, a two-path time-interleaved sampling scheme is employed to reduce the bandwidth requirement of the ADC driver. The associated schematic and timing diagram are shown in Fig. 7. In every clock cycle, one pair of sampling

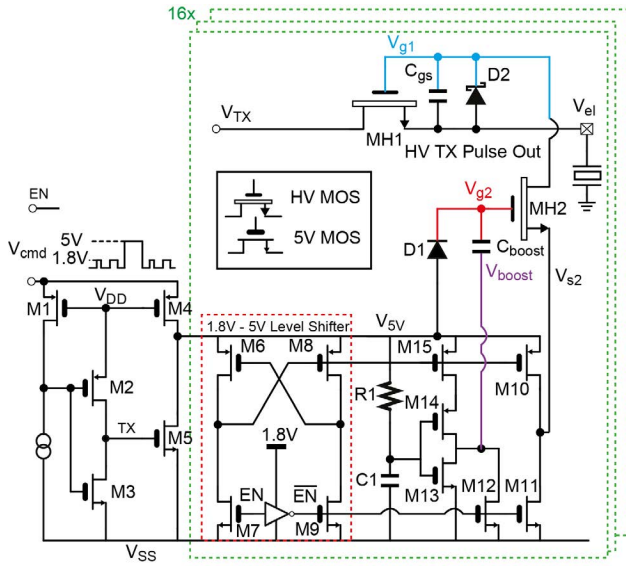


Fig. 10. Circuit diagram of the high-voltage switch and the control signal generator.

capacitors connects to ADC driver, making a full 16.6 ns available for settling, while the charge stored on the other pair is digitized.

C. Load-Modulation Datalink

To transmit the ADC's 10b output code through a single cable, a conventional implementation is to serialize the 10 b code using an oversampled clock generated on-chip with a power-hungry phase-lock-loop (PLL) or delay-lock-loop (DLL). Instead, to simplify the circuitry and reduce the on-chip power dissipation, the ADC output code is transmitted asynchronously by means of load modulation. Fig. 8 shows the principle. The comparator's asynchronous differential outputs COMP and COMN represent the output code. Two differently-sized NMOS load-modulation switches are driven by the comparator outputs, resulting in three different loads resistances. Together with a 50 Ω pull-up resistor on the system side, this forms a resistive divider on which a three-level waveform can be observed from which the ADC bits can be recovered. The supply voltage to which the pull-up resistor is connected is a trade-off between signal swing and power consumption. A voltage of 0.7 V was chosen experimentally (see Section IV.A), which leads to an on-chip power consumption associated with the data transmission of about 2.7 mW, comparable to the power consumption of the remaining building blocks.

D. High-Voltage Bootstrapped Switch

The HV switches serve to pass a transmit pulse generated by the imaging system to selected transducer elements during the TX phase. Earlier implementations of HV switches employ either level-shift circuits [22, 23] or bootstrapped capacitors [24] to provide overdrive to turn on a high-voltage MOS transistor. A level-shift circuit translates a low-voltage switch-control signal to the voltage level at which the switch operates, and tends to require a HV supply, which is not available in our system. A bootstrapped switch is a better match. It employs a capacitor at the gate of a HV MOS transistor which is charged

up to turn on the switch when the voltage level is low. The capacitor then maintains the overdrive when the voltage level increases, thus keeping the switch on. In [24], a switch is described that employs back-to-back connected transistors to provide bi-directional isolation. However, to turn on and off these transistors, two additional HV MOS transistors and several HV diodes are needed per switch, which requires significant die size.

In this work, we limit ourselves to unipolar pulses, so that back-to-back isolation is not required, allowing an implementation using only one HV switch transistor MH1 to connect the transmit element (V_{el}) to the off-chip HV pulser (V_{TX}), as shown in Fig. 9a. To turn on MH1, a bootstrap capacitor C_{gs} is charged to 5 V through transistor MH2. This happens when V_{TX} is still low, at the start of the TX phase. To turn on MH2, its gate voltage V_{g2} is pumped to approximately 10 V, while its source voltage V_{s2} is pushed to 5 V, as shown in Fig. 9b. The 10 V at the gate is generated by charging a capacitor C_{boost} to 5 V and then pushing the voltage V_{boost} at its bottom plate to 5 V. Because MH2 is now turned on, C_{gs} will be charged to V_{s2} (5 V). Once C_{gs} has been charged, MH2 is switched off by dropping V_{boost} , thus isolating the charge on C_{gs} and keeping MH1 switched on. HV transmit pulses on the TX line can then be passed to the transducer element. The bootstrap capacitor C_{gs} of 1.7 pF is sized such that MH1 maintains enough overdrive even if some charge is lost when the TX line goes high due to parasitic capacitance at node V_{g1} . A Zener diode D2 protects the gate of MH1. After the TX phase, MH1 is turned off by dropping V_{s2} , which causes C_{gs} to be discharged through MH2. A diode D1 then precharges C_{boost} for the next TX cycle. To prevent the switch from turning on during the TX phase, V_{boost} and V_{s2} are simply kept low, as illustrated in the second TX phase in Fig. 9b.

In order to generate the 5 V control signals V_{boost} and V_{s2} needed for the HV switch, a control signal generator is required, shown in Fig. 10. The required 5 V level is derived

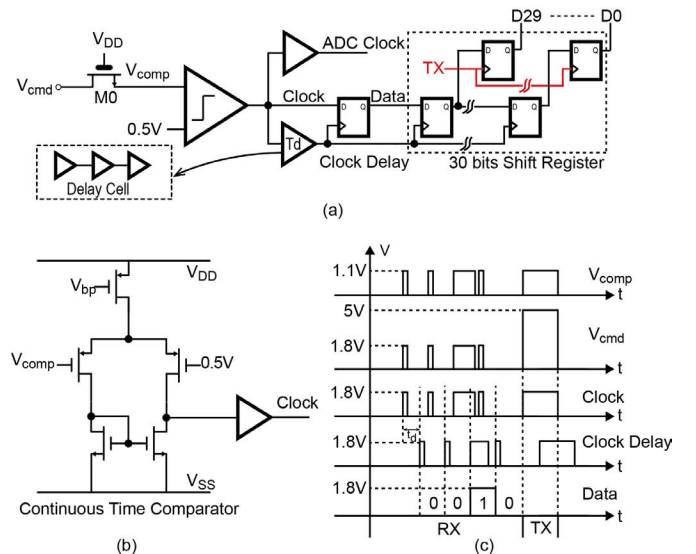


Fig. 11. Circuit diagrams of (a) clock and data recovery circuit; (b) the continuous-time comparator; (c) associated timing diagram.

from the COMMAND line. When the voltage V_{cmd} on that line is pulled to 5 V by the system to identify the start of the TX phase, M4 pulls the V_{SV} line up to 5 V. If V_{cmd} is between V_{SS} and V_{DD} , i.e. during the RX phase, this is detected by the circuit consisting of M1-3, which turns on M5 to pull V_{SV} to ground, completely turning off the HV switch circuit.

As said, the HV switch MH1 is turned on by pulling V_{boost} and V_{s2} to 5 V during the TX phase. Whether this happens is determined by a 1.8 V logic enable signal EN, provided by the chip's configuration shift register. With the help of a 1.8 V-5 V level shifter consisting of M6-9, this enable signal drives transistor M10 to pulling up V_{s2} . The shorter pulse on V_{boost} is generated by M12-15, R1 and C1, where the time required to charge C1 through R1 determines the duration of this pulse, which is set to approximately 20 ns. When EN is low, V_{s2} and V_{boost} are pulled down by M11 and M12, respectively, preventing the switch from turning on. Although the V_{SV} is pulled down to 0 V during the RX phase, the diode D1 prevents C_{boost} from being discharged.

E. Clock and Data Recovery Circuit

Besides providing a 5 V level during the TX phase, the COMMAND line also provides a clock for the ADC, and, in the form of PWM-encoded data, configuration bits that are loaded into a shift register to control the RX multiplexer, the gain of the AFE, and the EN signals of the TX switches. In order to recover the clock and data from the COMMAND line, the 5 V pulses are first clamped to protect the following low-voltage circuitry, and then, the extracted PWM signal is demodulated into a clock and data, as shown in Fig. 11a. A 5 V NMOS transistor M0 limits the V_{cmd} signal to $V_{DD} - V_{th}$, where V_{th} is the transistor's threshold voltage, after which a simple continuous-time comparator, shown in Fig. 11b, turns the signal into proper logic levels. The comparator is biased at 190 μ A to make sure that the latency of the comparator will not affect the duty cycle of recovered PWM signal. The rising edges of the resulting signal are used to trigger the ADC.

To decode the data bits, the signal level is sampled at half a clock cycle after the rising edge, as shown in Fig. 11c. To do so, a delayed version of the signal is used to clock a flip-flop.

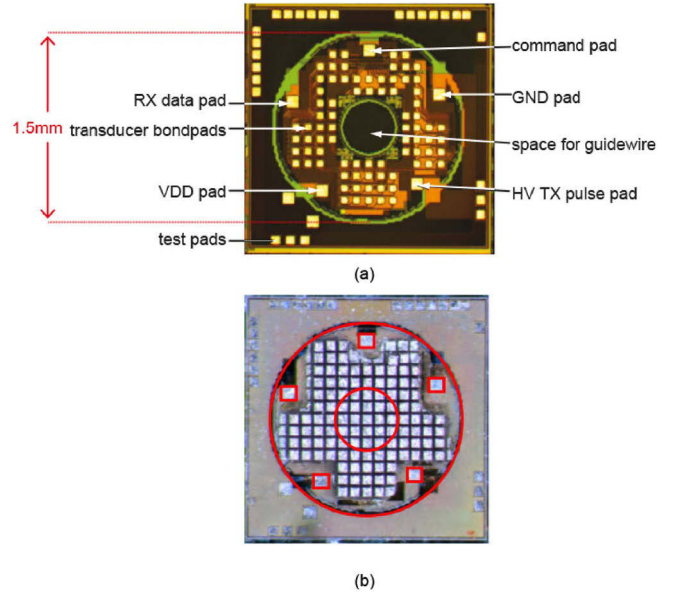


Fig. 12. (a) Chip micrograph (b) Micrograph of prototype ASIC with transducer array on top.

This delayed version is also used as the clock for the chip's 30-bit shift register. In order to prevent the current state of the shift register from being affected by the loading of new data into the shift register, the shift register output is buffered by a second set of flip-flops, which are clocked by the TX signal (obtained from the HV switch circuit, see Fig. 10). Thus, new configuration data only becomes active at the start of the succeeding TX phase.

IV. EXPERIMENTAL RESULTS

A. Experimental Setup

The ASIC has been realized in a 0.18 μ m high-voltage CMOS process with a total area of 2×2 mm², as shown in Fig. 12a. The circular layout has a 1.5 mm outer diameter and a central hole with a 0.5 mm diameter, so that it can be laser-cut into a donut shape to fit at the tip of a catheter. Five bond pads provide electrical connections for the four micro-coaxial

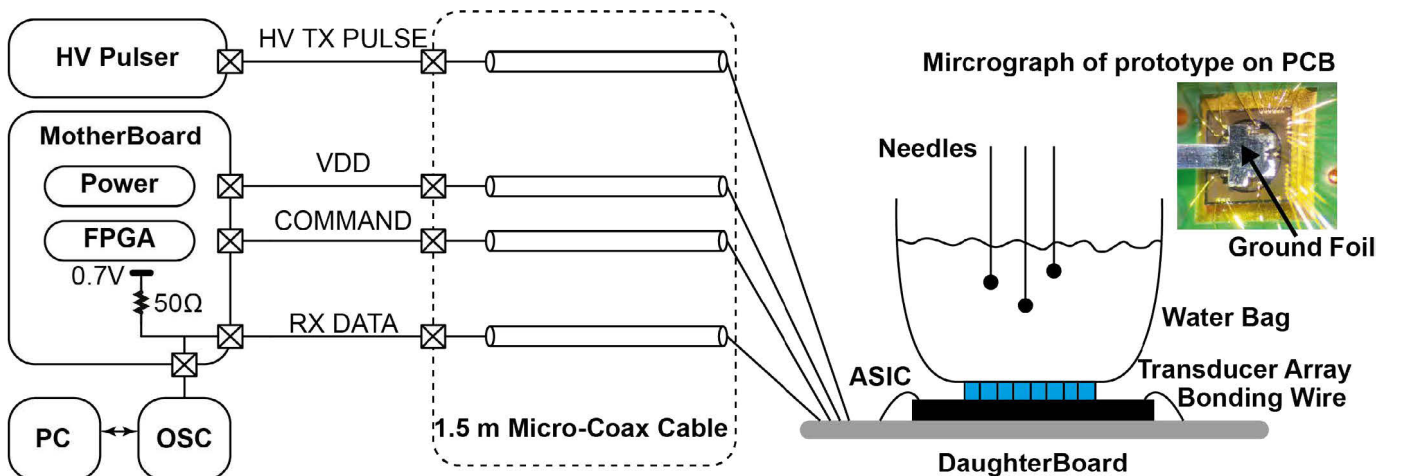


Fig. 13. Schematic diagram of the acoustical experimental setup.

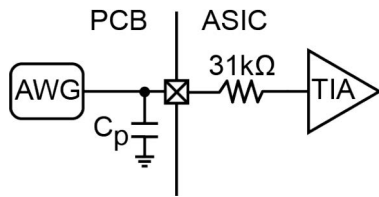


Fig. 14. Method of applying a test current to the TIA input.

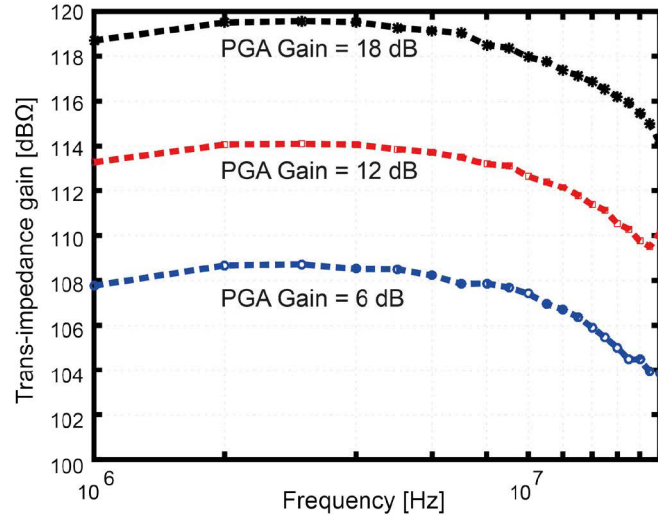


Fig. 15. Measured transfer function of the ASIC receive signal chain for different PGA gain settings.

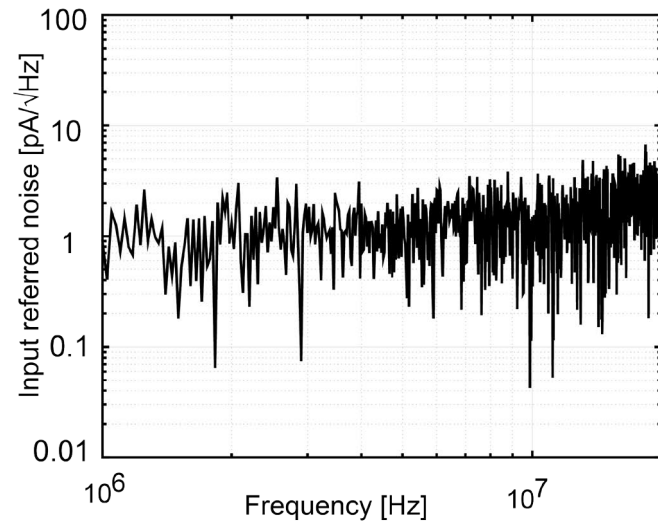


Fig. 16. Measured input-referred noise of the receive signal chain.

cables; 80 bond pads are positioned to connect to transducer elements. The die area around the donut is used for test circuits, which are not connected in the acoustical measurements reported below. These test circuits contain digital buffers that provide a parallel 10-bit ADC output (D_{out} in Fig. 5), as well as a test bondpad through which an electrical test signal can be applied to the analog front-end.

Fig. 12b shows a fabricated prototype with the transducer array built on top of the ASIC using the approach described in [19]. The bond pads on the ASIC that provide electrical connections to the transducer elements are equipped with gold

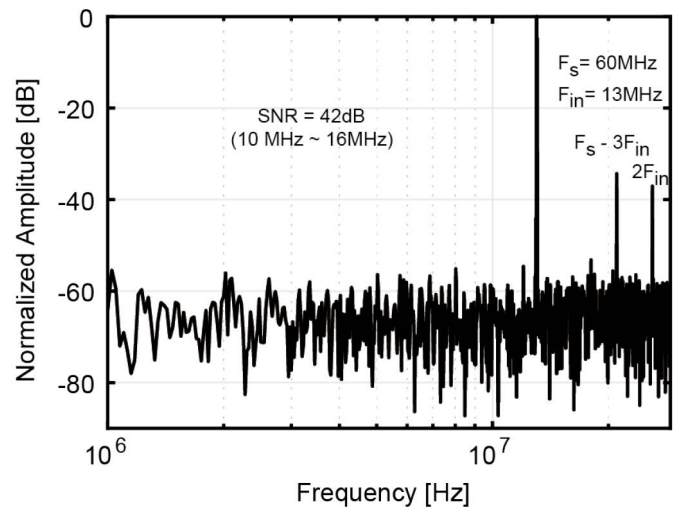


Fig. 17. Measured output spectrum of the receive signal chain for a 13 MHz sinusoidal input signal.

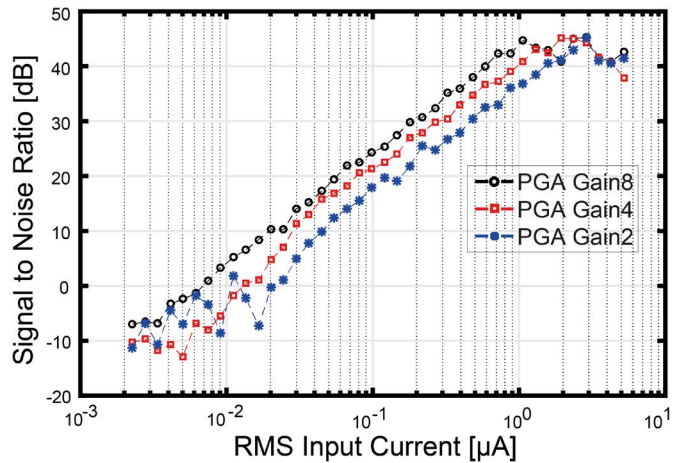


Fig. 18. Measured dynamic range of the ASIC receive signal chain for different PGA gain settings.

bumps using a wire-bonding tool. After this, an epoxy layer is applied to ASIC that is grinded down to expose the gold, thus providing reliable electrical contacts for the transducer elements. The acoustic stack consisting of a backing layer, a piezo-electric material (PZT) and a matching layer (with a total thickness of approximately 160 μm) is glued on top of the grinded epoxy layer, which is cut into the desired 100- μm -pitch array pattern using a diamond saw. Finally, the array is covered with an aluminium foil that forms the common ground electrode of the elements.

Fig. 13 shows a block diagram of the experimental setup. The ASIC is wire-bonded to a daughter board PCB. The ground foil is connected to the ground of the ASIC and the PCB. The ASIC's 4 cable connections are connected to four headers on the daughter board which are then connected through 1.5-m long micro-coaxial cables (AWG 42) to a mother board. The serial output of the ADC is captured by a high-speed oscilloscope with 1 GHz bandwidth (DL9710L, Yokogawa) and processed in MATLAB on a PC. The test signals are connected to the mother board through headers. The high-voltage pulse is provided by an external pulser

(AVTech, AVR40, Avtech Electrosystems Ltd.). The mixed-

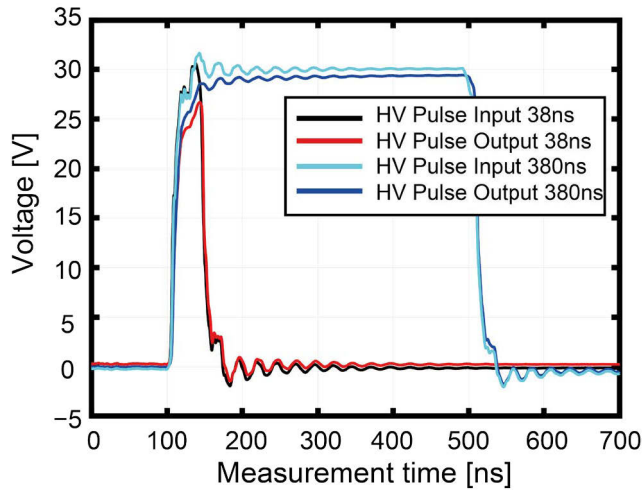


Fig. 19. Measured high voltage pulse input, and output at one TX transducer pad in different pulse width.

voltage multi-functional command line is generated by an FPGA and an analog switch (ADG719, Analog Device) which is used to pull the line to 5 V. The switch control signal and 60 MHz PWM signal are generated by the FPGA.

B. Electrical Measurements

In order to characterize the receive signal chain, an external test voltage was applied to the ASIC's analog test input, which is connected on chip via a 31 k Ω resistor to the TIA input to produce a test current, as shown in Fig. 14. This ensures that the parasitic capacitance (C_p) associated with the PCB trace and the on-chip bond pad do not affect the test current applied to the TIA. Fig. 15 shows the measured transfer function of the receive signal chain for the three gain settings. The measured trans-impedance gain ranges from 108 dB Ω to 119 dB Ω with a gain step of 5.7 dB Ω , and is 4-5 dB Ω lower than the design target because of the limited open-loop gain of the OTAs in the AFE.

The measured input-referred noise spectrum is shown in Fig. 16. The slight increase at higher frequencies is due to the roll-off of the transfer function (see Fig. 15). The total input-referred in-band (10 MHz to 16 MHz) rms noise is 4.8 nA in which the thermal noise of the 31 k Ω resistor is also included. While comparable to the 4.4 nA noise level of the transducer, this noise level is larger than the design target. A possible cause of this is coupling of the transient supply currents drawn by the ADC and the logic to the input of the LNA via the ground connection of the chip, which in this design also serves as the connection to the transducer's ground foil. This coupling can be reduced in the future by connecting the ground foil to the ground bond pad on the chip, rather than via the PCB.

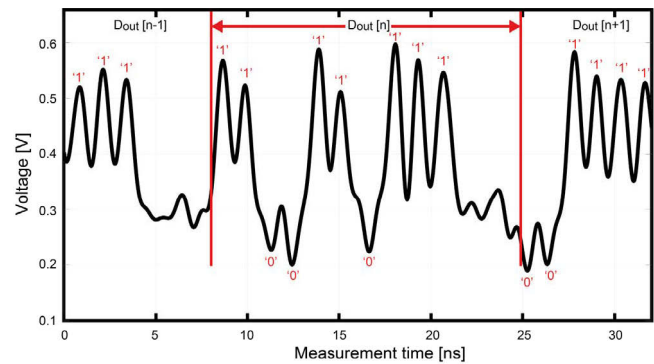


Fig. 20. Measured load modulation signal.

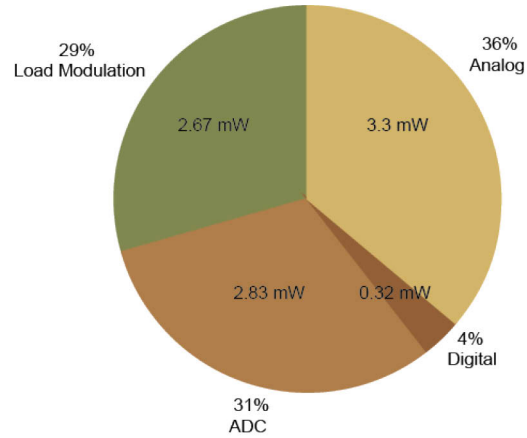


Fig. 21. Power breakdown of the chip.

A sinusoidal input signal was applied to evaluate the signal-to-noise ratio (SNR) and the linearity of the receive signal chain. The measured spectrum shown in Fig. 17 illustrates a 42 dB in-band (10MHz to 16MHz) SNR and \sim 37 dB HD2. The dynamic range measurement results are shown in Fig. 18. The measured dynamic range, accounting for the programmable gain, is around 53 dB, sufficient for the IVUS application.

The high-voltage switch was designed to transmit 30 V pulses at a frequency of 13 MHz (pulse width of 38 ns) for a PZT device with a parasitic capacitance of 0.7 pF. Fig. 19 shows the measured high-voltage pulse input and high-voltage pulse output of one selected channel in the high-voltage switch array. A 380 ns HV pulse is applied to show the highest voltage amplitude that the chip can provide, which is 29.3 V. A 38 ns pulse is also applied. The lower amplitude of the HV pulse output shown is caused by incomplete settling due to the large PCB parasitic. However, the transducer array used in the acoustical measurement is directly integrated on top of ASIC so that no additional parasitic are introduced and the HV pulse should be able to fully settle.

TABLE II. System-level comparison with prior work

	[13]	[14]	[6]*	This work
Transducer Type	CMUT	CMUT	PVDF	PZT
Process	0.35 μ m HV CMOS	0.35 μ m HV CMOS	3 μ m CMOS	0.18 μ m HV CMOS
Core chip size	1.4 mm \varnothing	2.1 mm \varnothing	4 \times (0.86 mm \times 1.65 mm)*	1.5 mm \varnothing
Supply voltage	3.3 V	3.3 V	10 V	1.9 V(V_{DD}) + 5 V(V_{cmd})
#Transmit	56	64	64	16
#Receive	48	56	64	64
Center frequency	20 MHz	12 MHz	20 MHz	13 MHz
Receive output	analog	analog	analog	digital
Receive bandwidth	40 MHz	n/a	27 MHz	16 MHz
Dynamic Range	50 dB	n/a	n/a	53 dB
Transmit circuit	pulser	pulser	pulser	switch
Max. transmit amplitude	25 V	12.5 V	10V	30 V
Power consumption	20 mW	n/a	30 mW	9.1 mW
Number of cables	13	13	7	4

* [6] is a side-looking IVUS design with 4 separate chips connected to a 64-element array.

Fig. 20 shows the load-modulation output captured using the high-speed oscilloscope. Compared to the ideal waveform shown in Fig. 8, the signal has clearly been low-pass filtered, partially due to the finite bandwidth of the oscilloscope. Nevertheless, the data bits can still be correctly extracted from the captured waveform. To do so, the captured waveform is first synchronized to the 60 MHz input clock and divided into chunks that corresponds to the 10 data bits of an individual sample. The data bits are then extracted by detecting the peaks in the waveform using MATLAB. By comparing the extracted data with the data captured from the parallel test outputs, a bit error rate (BER) of approximately 0.2% is found, which hardly affects the SNR.

Fig. 21 shows the power breakdown of the ASIC. The total power consumption is 9.1 mW, which is dominated by the power consumed by the ADC, the analog circuits (including the receive signal chain, the comparator in clock and data recovery circuits and the reference buffer) and the load modulation datalink.

C. Acoustic Measurements

To perform acoustic measurements, a water bag was mounted on top of the fabricated prototype, as shown in Fig. 14. Selected channels of the high-voltage transmit chain were excited and the pressure was measured using a hydrophone (SN1302, Precision Acoustics) suspended in the water 5 mm above the transducer array. The measured TX pressure for increasing number of excited elements is shown in Fig. 22a, showing, as expected, a peak pressure that increases roughly proportionally with the number of excited elements.

To test the receive functionality acoustically, a single element 5 MHz transmit transducer (PA865, Precision Acoustics) was placed under an angle in the water above the transducer array generating short acoustic pulses. Two receive

elements were selected to receive the acoustic signal as shown in Fig. 22b. The time delay between the recorded signals is consistent with the fact that the transmitter was placed at an angle, leading to different arrival time of the acoustic pulse on the two elements.

In order to show the 3D imaging capability of the prototype, a 3-needle phantom was placed in the water above the transducer array (Fig. 23a). The 16 transmit transducers were

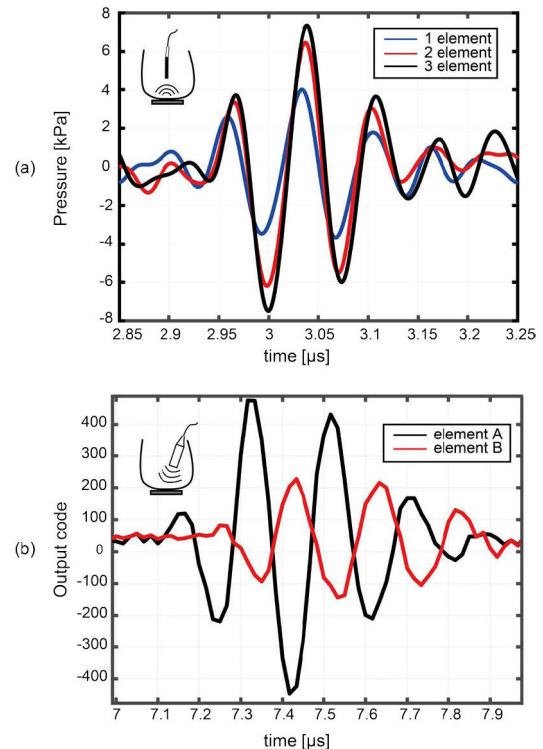


Fig. 22. (a) Measured TX pressure versus number of excited elements. (b) Receive signal measured through two transducer elements.

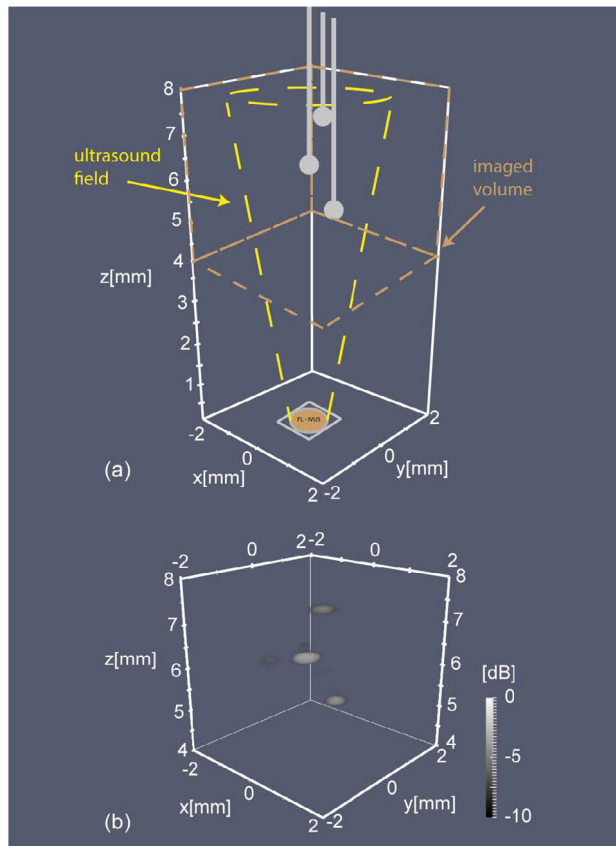


Fig. 23. (a) 3-needle phantom setup. (b) 3-D image showing the position of the 3 needles.

excited simultaneously by 30-V pulses of 30 ns to generate a TX beam. The echo signals from 64 receive transducers were then recorded sequentially. A 3D image showing a dynamic range of 10 dB (Fig. 23b) was reconstructed by means of delay-and-sum beamforming of the received echo signals. The three needle heads can be clearly recognized in the image. For the central needle, side-lobe artifacts are visible close to the main signal. These artifacts are present for all the needles but since the central needle reflects most of the signal, only there the artifact is visible in the 10 dB dynamic range image. Note that better image quality can be obtained by employing synthetic aperture also in TX, and by applying more sophisticated reconstruction techniques. This, however, is beyond the scope of this paper.

A comparison of our ASIC performance and characteristics with the prior art is provided in Table I. The designs described in [13] and [14] employ ring-shaped CMUT transducer arrays with separate RX and TX elements. The on-chip circuitry includes per-element receive amplifiers, multiplexers and buffers that provide 4 parallel receive outputs, as well as pulsers with the associated control logic. The design described in [6] is for a side-looking IVUS probe, in which four ASICs are connected to a 64-element PVDF array. Each ASIC includes 16 receive amplifiers and transmit pulsers, with a single differential current-mode receive output shared by the four ASICs. A unique feature of our work is that it not only includes a receive front-end, but also an ADC and a load-

modulation datalink. Rather than employing on-chip pulsers, we use on-chip high-voltage switches, which connect selected TX elements to a pulser on the system side, thus reducing the on-chip power dissipation. Our ASIC features the lowest cable count and the lowest power consumption, and is the first to provide a digitized output signal.

V. CONCLUSION

This paper has presented a front-end ASIC for 3D intravascular ultrasound imaging which interfaces with 16 transmit elements and 64 receive elements using only four 1.5 m micro-coaxial cables. The chip has 1.5 mm diameter donut-shaped lay-out to facilitate placement around the guidewire of a catheter. A multi-functional mixed-voltage command line is used to transmit clock, data and a power supply for the HV switches through only one cable. A load-modulation-based data transmission scheme is used to transfer the ADC's 10-b output asynchronously through one cable. A high-voltage switch array with a compact and power-efficient circuit-level implementation allows 16 transmit transducers to be excited through one cable. To overcome the challenges of limited area- and power-constraints, an inverter-based analog front-end and a charge-sharing SAR ADC have been implemented. The effectiveness of these techniques has been successfully demonstrated in a 3D ultrasound imaging experiment.

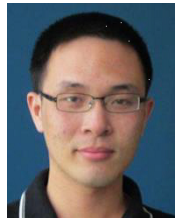
REFERENCES

- [1] R. Ross, "Mechanisms of disease - Atherosclerosis - An inflammatory disease," *New England Journal of Medicine*, vol. 340, pp. 115-126, Jan. 1999.
- [2] "Cardiovascular Diseases (CVDs)," World Health Organization, May 2017. [Online]. Available: <http://www.who.int/mediacentre/factsheets/fs317/en/>.
- [3] H. Garcia-Garcia, M. A. Costa, and P. W. Serruys, "Imaging of coronary atherosclerosis: intravascular ultrasound," *European Heart Journal*, vol. 31, no.20, pp. 2456-2469, Sep. 2010.
- [4] P.G. Yock, "Catheter apparatus, system and method for intravascular two-dimensional ultrasonography," U.S. Patent 4 794 931, Jan 3, 1989.
- [5] M. O'Donnell *et al.*, "Catheter arrays: Can intravascular ultrasound make a difference in managing coronary artery disease," in *Proc. IEEE Int. Ultrason. Symp.*, vol. 2, pp. 1447-1456, 1997.
- [6] W. C. Black and D. N. Stephens, "CMOS Chip for Invasive Ultrasound Imaging," *IEEE J. Solid-State Circuits*, vol. 29, no. 11, pp. 1381-1387, Nov. 1994.
- [7] L. Gatzoulis *et al.*, "Three-dimensional forward-viewing intravascular ultrasound imaging of human arteries in vitro," *Ultrasound in Medicine & Biology*, vol. 27, pp. 969-982, July 2001.
- [8] S. G. Aziz and D. R. Ramsdale, "Chronic total occlusions—a stiff challenge requiring a major breakthrough: is there light at the end of the tunnel?" *Heart*, pp. 42-48, 2005.
- [9] B. K. Courtney, N. R. Munce, *et al.*, "Innovations in imaging for chronic total occlusions: a glimpse into the future of angiography's blind-spot," *European Heart Journal*, vol. 29, no. 5, pp. 583-593, 2008.
- [10] J. L. Evans, K. H. Ng, M. J. Vonesh, B. L. Kramer, S. N. Meyers, T. A. Mills, *et al.*, "Arterial imaging with a new forward-viewing intravascular ultrasound catheter, I. Initial studies," *Circulation*, vol. 89, pp. 712-7, Feb. 1994.
- [11] K. H. Ng, J. L. Evans, M. J. Vonesh, S. N. Meyers, T. A. Mills, B. J. Kane, *et al.*, "Arterial imaging with a new forward-viewing intravascular ultrasound catheter, II. Three-dimensional reconstruction and display of data," *Circulation*, vol. 89, pp. 718-23, Feb. 1994.
- [12] J. H. Rogers, "Forward-looking IVUS in chronic total occlusions," *Cardiac Interventions Today*, pp. 21-24, 2009.

- [13] G. Gurun, et al., "Single-chip CMUT-on-CMOS front-end system for real-time volumetric IVUS and ICE imaging," *IEEE Trans. Ultrason. Ferroelectr. Freq. Control*, vol. 61, no. 2, pp. 239-250, Feb. 2014.
- [14] C. Tekes, T. Xu, T. M. Carpenter, S. Bette, U. Schnakenberg, D. Cowell, et al., "Real-Time Imaging System using a 12-MHz Forward-Looking Catheter with Single Chip CMUT-on-CMOS Array," in *Proc. IEEE Int. Ultrason. Symp.* 2015.
- [15] E.D. Light, and S. W. Smith. "Two-dimensional arrays for real-time 3D intravascular ultrasound," in *Ultrasonic Imaging*, vol. 26, pp. 115-128, 2004.
- [16] G. Gurun, P. Hasler, and F. L. Degertekin, "Front-End Receiver Electronics for High-Frequency Monolithic CMUT-on-CMOS Imaging Arrays," *IEEE Trans. Ultrason., Ferroelectr., Freq. Control*, vol. 58, no. 8, pp. 1658-1668, Aug. 2011.
- [17] J. Lim, C. Tekes, F. L. Degertekin, and M. Ghovanloo, "Towards a Reduced-Wire Interface for CMUT-Based Intravascular Ultrasound Imaging Systems," *IEEE Transactions on Biomedical Circuits and Systems*, vol. 11, no. 2, pp. 400-410, Apr. 2017.
- [18] M. Tan et al., "A front-end ASIC with high-voltage transmit switching and receive digitization for forward-looking intravascular ultrasound," in *Proc. IEEE Custom Integrated Circuits Conference (CICC)*, 2017, pp. 1-4.
- [19] C. Chen, S. B. Raghunathan, Z. Yu, M. Shabanmoghlagh, Z. Chen, Z. Y. Chang, et al., "A Prototype PZT Matrix Transducer With Low-Power Integrated Receive ASIC for 3D Transesophageal Echocardiography," *IEEE Trans. Ultrason., Ferroelectr., Freq. Control*, vol. 63, pp. 47-59, Jan. 2016.
- [20] Y. Wang, D. N. Stephens and M. O'Donnell, "Optimizing the Beam Pattern of a Forward-Viewing Ring-Annular Ultrasound Array for Intravascular Imaging," *IEEE Trans. Ultrason., Ferroelectr., Freq. Control*, vol. 49, no. 12, pp. 1652-1664, Dec. 2002.
- [21] T. L. Szabo, *Diagnostic Ultrasound Imaging: Inside out*, pp 387-388, Elsevier, 2004.
- [22] H.-K. Cha, D. Zhao, J.H. Cheong, B. Guo, H. Yu, and M. Je, "A CMOS high-voltage transmitter IC for ultrasound medical imaging applications," *IEEE Trans. Circuits Syst. II: Express Briefs*, vol. 60, no. 6, pp. 316-320, June 2013.
- [23] D. Zhao et al., "High-voltage pulser for ultrasound medical imaging applications," in *Proc. 13th Int. Symp. Integrated Circuits (ISIC)*, pp. 408-411, 2011.
- [24] K. Hara, et al. "A New 80V 32x32ch low loss multiplexer LSI for a 3D ultrasound imaging system," in *Proc. Int. Symp. on Power Semiconductor Devices and ICs*, pp. 359-362, May 2005.
- [25] J. W. Choe, et al., "Volumetric real-time imaging using a CMUT ring array," *IEEE Trans. Ultrason., Ferroelectr., Freq. Control*, vol. 59, no. 6, pp. 1201-1211, June 2012.
- [26] Y. Chae and G. Han, "Low voltage, low power, inverter-based switched capacitor delta-sigma modulator," *IEEE J. Solid-State Circuits*, vol. 44, no. 2, pp. 458-472, Feb. 2009.
- [27] R. Carvajal, et al., "The flipped voltage follower: a useful cell for low-voltage low-power circuit design," *IEEE Trans. Circuits Syst. I, Reg. Papers*, vol. 52, no. 7, pp. 1276-1291, July 2005.
- [28] K. Kaviani, O. Oralkan, P. Khuri-Yakub, and B. A. Wooley, "A multichannel pipeline analog-to-digital converter for an integrated 3-D ultrasound imaging system," *IEEE J. Solid-State Circuits*, vol. 38, no. 7, pp. 1266-1270, July 2003.
- [29] M. K. Chirala, P. Huynh, J. Ryu, and Y. H. Kim, "A 128-ch Delta-Sigma ADC based Mixed Signal IC for full Digital Beamforming Wireless Handheld Ultrasound Imaging System," *2015 37th Annual International Conference of the IEEE Engineering in Medicine and Biology Society (EMBC)*, pp. 1339-1342, 2015.
- [30] M. C. Chen et al., "A Pixel Pitch-Matched Ultrasound Receiver for 3-D Photoacoustic Imaging With Integrated Delta-Sigma Beamformer in 28-nm UTBB FD-SOI," *IEEE J. Solid-State Circuits*, vol. 52, no. 11, pp. 2843-2856, Nov. 2017.
- [31] B. Malki, et al. "A 70 dB DR 10 b 0-to-80 MS / s current-integrating SAR ADC with adaptive dynamic range," *IEEE J. Solid State Circuits*, vol. 49, no. 5, pp. 1173-1183, May 2014.
- [32] A.M. Abo and P. R. Gray, "A 1.5-V, 10-bit, 14.3-MS/s CMOS pipeline analog-to-digital converter," *IEEE J. Solid-State Circuits*, vol. 34, no. 5, pp. 599-606, May 1999.



His research interests include analog and mix-signal electronics, especially for bio-medical applications.



Butterfly Network Inc., Guilford, CT, USA, where he designs ASICs for next-generation medical ultrasound systems. His current research interests include integrated circuits for medical ultrasound imaging, low power sensor interfaces, and data converters.

Mr. Chen was a recipient of the Huygens Scholarship in 2011. He was also a recipient of the ISSCC 2013 STGA award, the winner of IEEE IUS 2017 student paper competition award and a co-recipient of the A-SSCC 2017 best student paper award.



Mingliang Tan received the B.S. degree in electronic science and technology from Northeastern University, Shenyang, China, in 2014, and M.S. degree in microelectronics from Delft University of Technology, Delft, The Netherlands, in 2016. He is currently pursuing the Ph.D degree in electrical engineering at the Electronic Instrumentation Laboratory, Delft University of Technology, where he works on ASIC design for medical ultrasound imaging.

Chao Chen received the B.Sc. degree from Tsinghua University, Beijing, China, in 2010, the M.Sc. degree (*cum laude*) from the Delft University of Technology, Delft, The Netherlands, in 2012, and the Ph.D. degree from the Delft University of Technology, Delft, the Netherlands, in 2018, all in microelectronics.

His Ph.D. research topic was front-end ASIC design for 3-D medical ultrasound imaging. Since November 2017, he has been a senior analog IC designer with

Zhao Chen received the B.S. degree in microelectronics from Fudan University, Shanghai, China, in 2011, and the M.S. degree in electrical and electronic engineering from Imperial College, London, U.K., in 2012. He is currently pursuing the Ph.D degree in electrical engineering at Delft University of Technology, Delft, The Netherlands. The research during his doctoral study is on the ASIC design for 3-D medical ultrasound imaging.

His research interests include analog and mixed-signal electronics, especially for biomedical application.



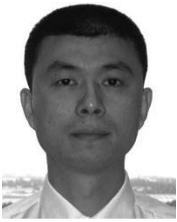
Rotterdam, The Netherlands.

Her research interests include intravascular ultrasound imaging, transducer design and evaluation.



Jovana Janjic received the B.Sc. in Information Engineering in 2011 and the M.Sc. in Bioengineering in 2013 from The University of Padova, Italy. She was selected within the Erasmus Programme as an exchange student at the Royal Institute of Technology (KTH), Stockholm, Sweden, from August 2012 until June 2013. At KTH she completed her Master thesis on sonothrombolysis using contrast agents. She is currently pursuing the Ph.D. degree in Biomedical Engineering at the Erasmus MC,

Verrya Daeichin was born in Kermanshah, Iran, in 1984. He received the bachelor's degree in bioelectric engineering from the Biomedical Engineering Department at Amirkabir University of Technology (Tehran Polytechnic) in 2008. In 2009, he finished his first master's degree in biomedical signal processing and pattern recognition from University of Boras in Sweden. His second master's degree was from Chalmers University of Technology in biomedical image processing. Since 2010, he has been a Ph.D. candidate at Erasmus MC, Rotterdam, The Netherlands. His research area is molecular imaging using target microbubbles contrast agents.



Zu-yao Chang received the M.Sc. degree in electrical engineering from Delft University of Technology, Delft, The Netherlands, in 2003. Since 2003, he has been a Staff Member with the Electronic Instrumentation Laboratory, Delft University of Technology, working on impedance measurement systems and smart sensor systems.



Emile Noothout graduated from Intermediate Technical School for Mechanics, Dordrecht, The Netherlands, in 2004. Then, he studied for Research Instrument Maker at Leidse Instrumentmaker School, Leiden, The Netherlands, from 2004 to 2006.

From 2007 to 2013, he worked as a Research Instrument Maker with TNO, Delft, The Netherlands. Since 2013, he has been working with Delft University of Technology, Delft, The Netherlands, for the development of medical

ultrasound transducers and research assistance.



Gijs van Soest received his M.Sc. degree in physics in 1997 from the University of Groningen. He then moved to the University of Amsterdam, where he obtained his Ph.D. degree for research on the interplay of light scattering and laser physics in December 2001. Between 2002 and 2005, he worked on remote sensing of atmospheric trace gases and satellite validation at the Royal Netherlands Meteorology Institute and the Space Research Organization of the Netherlands.

In 2005, he joined the Thoraxcenter in a postdoctoral position, for a project on OCT elastography. Since then, his activities have broadened to include catheter development, automatic image analysis, and high-frequency ultrasonic imaging. In January 2010, he was appointed Assistant Professor and became a staff member of the Department of Biomedical Engineering.

His research focuses on the use and development of intravascular imaging methods for detection of coronary atherosclerosis. He is currently working on optical coherence tomography, specifically on methods for functional imaging, and on intravascular photo-acoustic imaging. These developments are carried out in close collaboration with clinicians of the Department of Interventional Cardiology.



Martin D. Verweij (M'10) received the M.Sc. (cum laude) and Ph.D. degrees in electrical engineering from Delft University of Technology, Delft, The Netherlands, in 1988 and 1992, respectively. From 1993 to 1997, he was a Research Fellow with the Royal Netherlands Academy of Arts and Sciences, Amsterdam, The Netherlands. In 1998, he became an Associate Professor with the Laboratory of Electromagnetic Research, Delft University of Technology, where he joined the Laboratory of

Acoustical Wavefield Imaging in 2011. His research interests include dedicated transducer design, beamforming algorithms, and the theoretical modeling and numerical simulation of medical ultrasound. Dr. Verweij is an Associate Editor of the Journal of the Acoustical Society of America.



Nico de Jong (A'97–M'09) received the M.Sc. degree in physics from Delft University of Technology, The Netherlands, in 1978 and the Ph.D. degree for "Acoustic properties of ultrasound contrast agents" from the Erasmus Medical Center, Rotterdam, The Netherlands, in 1993.

Since 1980, he is a Staff Member with the Thoraxcenter, Erasmus Medical Center, Rotterdam, The Netherlands. In 2003, he became a part-time Professor with the University of Twente, Enschede,

The Netherlands. Over the last 5 years, he has given more than 30 invited lectures and has given numerous scientific presentations for international industries. He teaches on Technical Universities and the Erasmus MC. He has been the promotor of 21 Ph.D. students and is currently supervising 11 Ph.D. students. Since October 2011, he is a Professor in Molecular Ultrasonic

Imaging and Therapy with the Erasmus MC and the Technical University of Delft, Delft, The Netherlands.

Dr. de Jong is an Organizer of the annual European Symposium on Ultrasound Contrast Imaging, held in Rotterdam and attended by approximately 175 scientists from universities and industries all over the world. He is on the safety committee of World Federation of Ultrasound in Medicine and Biology (WFUMB), Associate Editor of UMB, and has been Guest Editor for special issues of different journals.



Michiel A. P. Pertijs (S'99–M'06–SM'10) received the M.Sc. and Ph.D. degrees in electrical engineering (both *cum laude*) from Delft University of Technology, Delft, The Netherlands, in 2000 and 2005, respectively. From 2005 to 2008, he was with National Semiconductor, Delft, where he designed precision operational amplifiers and instrumentation amplifiers. From 2008 to 2009, he was a Senior Researcher with imec / Holst Centre, Eindhoven, The Netherlands. In 2009, he joined the Electronic

Instrumentation Laboratory of Delft University of Technology, where he is now an Associate Professor. He heads a research group focusing on integrated circuits for medical ultrasound and energy-efficient smart sensors. He has authored or co-authored two books, three book chapters, 12 patents, and over 90 technical papers.

Dr. Pertijs served as an Associate Editor of the IEEE Journal of Solid-State Circuits (JSSC). He is a member of the technical program committee the European Solid-State Circuits Conference (ESSCIRC), and also served on the program committees of the International Solid-State Circuits Conference (ISSCC) and the IEEE Sensors Conference. He received the ISSCC 2005 Jack Kilby Award for Outstanding Student Paper and the JSSC 2005 Best Paper Award. For his Ph.D. research on high-accuracy CMOS smart temperature sensors, he received the 2006 Simon Stevin Gezel Award from the Dutch Technology Foundation STW. In 2014, he was elected Best Teacher of the EE program at Delft University of Technology.